Numerical Analysis of Blast Furnace Hearth Drainage Based on a Simulated Hele–Shaw Model

Liu, Weiqiang; Shao, Lei; Saxén, Henrik

Published in:
Steel Research International

DOI:
10.1002/srin.202100629

Published: 01/06/2022

Document Version
Accepted author manuscript

Document License
Publisher rights policy

Numerical Analysis of Blast Furnace Hearth Drainage Based on a Simulated Hele-Shaw Model

Weiqiang Liu,[1] Lei Shao[2*], Henrik Saxén[1*]

1. Process and Systems Engineering Laboratory, Faculty of Science and Engineering, Åbo Akademi University, Åbo 20500, Finland
2. School of Metallurgy, Northeastern University, Shenyang 110819, China.

*) Corresponding author, Lei Shao: shaolei@mail.neu.edu.cn
*) Corresponding author, Henrik Saxén: Henrik.Saxen@abo.fi

Abstract: For a modern blast furnace, a smooth tapping is a key prerequisite to keep the furnace running efficiently. An understanding of the hearth drainage and the influence of associated operational factors is therefore vitally important. To investigate the hearth tapping, a two-dimensional computational fluid dynamics (CFD) model was developed and verified based on results from an experimental Hele-Shaw model. A series of simulation cases was conducted with the CFD model, studying the effect of the blast pressure, packed bed permeability, coke-free zone, and initial accumulated amounts of liquids on the tapping behavior, using water and oil as liquids as in the experimental model. To quantify the simulation findings, the effect of the above process conditions on the evolution of some drainage parameters, i.e., the liquid levels and volumes, flow rates, ratio of oil and water in the outflow, as well as angle of the interfaces were analyzed. The results reveal interesting findings about the hearth drainage and also show similarities with the outflow patterns of the hearth liquids in operating blast furnaces.

Keywords: blast furnace, hearth drainage, iron and slag flow, numerical simulation

1. Introduction

The blast furnace (BF) is the primary ironmaking unit supplying molten iron for the steelmaking in the downstream processes. As one of the core parts of it, the hearth works as a temporal storage of the main product, hot metal, and the by-product, slag, which pass through the packed coke bed (deadman) and are drained through the taphole. Modern big BFs have three or four tapholes, but usually only two of them are employed alternately.[1] The tapping is started by drilling a hole in the hearth sidewall lining and is ended by plugging the hole with mud. A smooth hearth drainage is essential for achieving an efficient and stable running of the BF and for reducing splashing and wear of the taphole and the runner.

The drainage shows three types of outflow patterns, i.e., iron only, slag only, and a simultaneous flow of iron and slag, which depend on the phases in contact with the entrance of the taphole channel. Commonly, the simultaneous outflow dominates, while the single-phase outflow may appear at the start of the tapping. The simultaneous outflow of iron and slag can occur if the main iron-slag interface inside the hearth is slightly above, at, or (even well) below the level of the taphole entrance. When this interface is slightly above the taphole, the pressure drop caused by the iron flow in the packed bed may "pump" slag from above into the taphole, but this effect is not strong due to the low viscosity of the iron. By contrast, the flow of the viscous slag through the packed bed creates a significant pressure gradient near the taphole, which can lift and drain iron from the levels far below the taphole entrance.[2–6] As the tap is approaching its end, also the local slag-gas interface starts bending. Thus both the slag-gas and iron-slag interfaces bend towards the taphole but in opposite directions, and the tap is typically ended when the former interface reaches the taphole and gas starts bursting out. For some cases, a non-smooth slag-gas interface may appear, due to *viscous fingering* as a result of local variations of the deadman permeability, causing premature outburst of gas.[7] While the simultaneous outflow of the hearth liquids occurs at the later part of the tap, the outflow

conditions at the start of the tap vary, mainly depending on the initial level of the iron-slag interface. If the iron-slag interface is well above the taphole, the tapping starts with iron-only flow, but as the interface descends due to the iron outflow, the simultaneous flow pattern occurs and typically prevails until the end of the tap. If, by contrast, the iron-slag interface is well below the taphole, the tap starts with slag-only flow. As the outflow gets strong enough, or when the iron-slag interface rises sufficiently due to the supply of iron from the upper part of the BF, a point is reached where the pressure gradient is sufficient to lift the iron to the taphole, yielding a simultaneous outflow that prevails until the end of the tap. A further complication is the possibility that the deadman coke floats due to the buoyancy of the hearth liquids, which can influence the liquid levels during the tapping, and an asymmetric distribution of the deadman voidage can further give rise to spatial variation of the liquid levels which affects the drainage.[8] In summary, the BF tapping is very complex and is influenced by many factors. Since it is difficult to obtain information from the BF hearth because of the hostile environment, numerical and experimental models are beneficial tools for studying BF hearth drainage.

Several investigations of BF hearth drainage based on experimental cold models and numerical models have already been undertaken. Tanzil et al. first revealed that it is possible to drain the denser liquid from a level well below the outlet in physical two-dimensional (2D) and three-dimensional (3D) models,[2,3] which revised earlier assumptions.[9] Zulli extended the work to consider the influence of a coke-free zone on the drainage.[4] By employing experimental Hele-Shaw models and a 3D model, the effect of packing pattern, coke-free region, initial amount of the liquids, etc. on the liquid interfaces, outflow patterns, gas breakthrough time have been investigated by several authors.[7,10-12] For gaining a deeper understanding of hearth drainage, some computational models have also been established. Nouchi et al.[13] developed a simplified mathematical model to quantify the effects of some operational factors (such as production rate, initial taphole opening level, and low permeability zone) on the liquid

levels and liquid outflow ratio. Iida et al.[14] established a multi-pool model including low-permeability zones in the packed coke bed to study and explain possible reasons for the asymmetric drainage of slag observed in BFs with two alternating tapholes. Later, Roche et al.[15] demonstrated that an asymmetric outflow of slag can be caused by differences in the local permeability of the coke bed in front of the tapholes, which yield fluctuating liquid levels resulting in iron only and slag only flow at the start of the taps from the two alternating tapholes. Some online estimation models have also been developed and employed for explaining the hearth tapping phenomena. Brännbacka et al.[16] developed a simplified online model for estimation of the liquid levels in the hearth based on measured information about the outflows, assuming that the deadman is sitting. Later this model was extended to a more advanced version considering time-varying hearth profile and deadman floating.[17] Roche et al.[18] developed a multi-pool liquid online model to consider drainage differences of the alternating tapholes of a large three-taphole BF.

To gain more detailed and comprehensive process information, some computational fluid dynamics (CFD) models, or models combing CFD with the discrete element method for the coke phase (CFD-DEM) have also been developed and employed for studying the BF hearth drainage. Nishioka et al.[19,20] developed a three-dimensional CFD model verified by industrial data. The model was run to a quasi-stationary state to study the influence of a series of furnace operation conditions on the evolution of interface levels, average slag thickness, and drainage rates in a BF with alternating tapping. Shao and Saxén[5] proposed an improved two-fluid (TF) model to simulate iron and slag tapping in the hearth, comparing it with the well-established volume of fluid (VOF) model both for the iron-slag and water-oil systems. The study showed that a more reliable prediction of single drainage rates can achieve by using the TF model. To study the interface deformation of the gas-liquid flow in the hearth, Park et al.[21,22] developed a two-phase 3D CFD model. The model demonstrated that *viscous fingering* may occur as the

liquid-gas interface was near the outlet during the simulation. Kaymak et al.[23] developed a simplified 3D CFD model to simulate the tilting of both slag-gas and slag-iron interfaces during the hearth tapping process. To reduce the computational load, instead of the common used multiphase flow model, a single slag phase flow in coke packed bed with two moving interfaces has been formulated and implemented in this model where the interface movements were modelled by the moving mesh physics. Vångö et al.[24] established an unresolved CFD-DEM model considering the dynamic behavior of the particle bed, where the flow around each particle is not solved. The model, which was validated by a drainage experiment, was employed to simulate the tapping of molten iron and slag in a small-scale BF hearth.

A common problem of experimental and numerical studies of BF hearth drainage in the literature is that they report results under strongly limited conditions and usually only for a few runs. By contrast to 3D models, a 2D Hele-Shaw model combined with a method for automatic image processing[12,25,26] is an ingenious experimental device by which hearth drainage can be quantified and visualized, but it is still quite toilsome to undertake the experiments because the slot model has to be carefully cleaned between the experiments (to remove oil that sticks to the glasses). Furthermore, it is not easy to examine the effect of certain factors, like coke-free zone and permeability of the packed bed. Considering these challenges and the advantages, including low labor cost, ease to change the geometry and conditions, a VOF-based CFD model was established to simulate the tapping of a Hele-Shaw model that was used in the earlier work by the authors[12,25,26] to theoretically verify the experimental findings and to complement them. For the VOF method, appropriate computational grid size and arrangement are essential to describe the interface shape accurately. Thus for this model, the grid resolution was assigned carefully, especially for the region close to the outlet channel, and mesh dependency was also checked. The model was first validated by comparison with experimental data and then applied to examine the influence of several factors on the liquid levels and volumes, outflow rates, and

interface bending. This provides a “clean view” of the conditions which is not as much influenced by non-ideal and stochastic terms as the experimental model, where the small outlet and the piping turned out to give rise to complex effects on the overall pressure drop (as illustrated in the Appendix of ref. [26]). Section 2 of the paper provides details of the CFD model. Section 3 presents the model validation and the cases simulated, followed by a section discussing the findings. The fifth and final section concludes the paper by summarizing the findings and proposing directions of future work.

2. Model Description

2.1. Assumptions and Simplifications

To describe the drainage of the two fluids, water and oil, mimicking iron and slag, in a Hele-Shaw cell, a CFD model (**Figure 1**) was established. The modeling is based on the following fundamental assumptions and simplifications:

(a) Air, water, and oil are incompressible fluids with constant density and viscosity.

(b) Heat transfer is not considered and the temperature is kept fixed (at 21 °C).

(c) Effects of capillary forces and surface tension are neglected.

(d) The main domain is a fixed and homogenous 2D packed bed and a flow resistance term is introduced to simulate the viscous flow in the Hele-Shaw cell based on the viscous flow analogue.[2]

(e) The fluids are pre-filled in the model before the simulation and the simulation is stopped when air enters the outlet channel.

(f) No liquids are added to the system during the drainage.

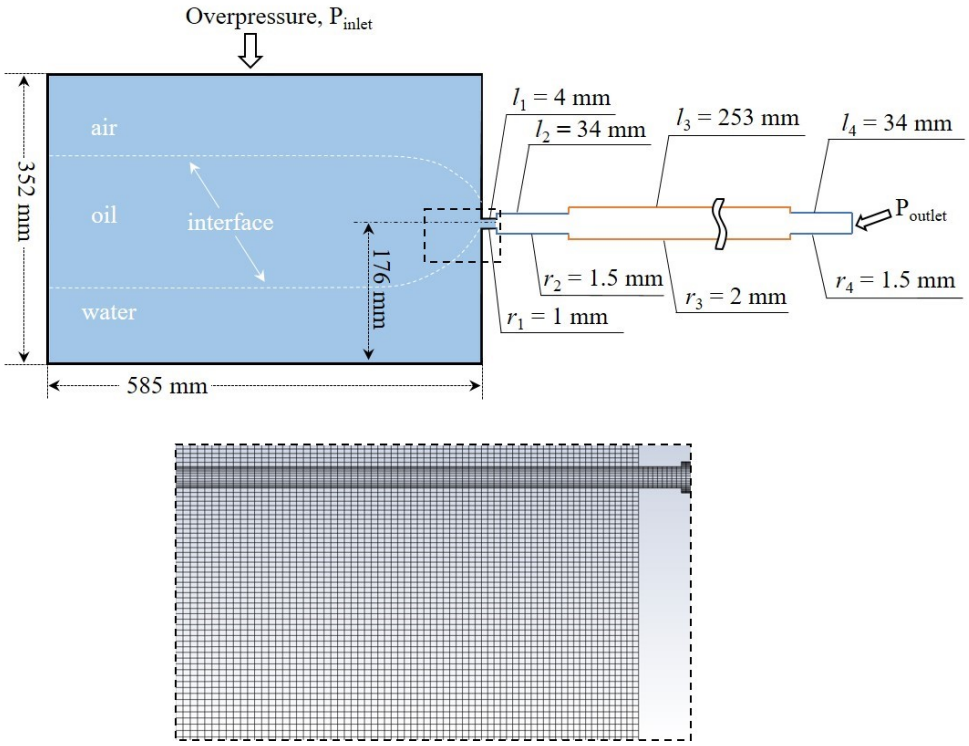

Figure 1. Upper panel: Schematic of the CFD drainage model. Lower panel: Mesh resolution for the local region close to the outlet.

2.2 Model Equations

The VOF model is applied to track the liquid-gas (l-g) and liquid-liquid (l-l) interfaces during the tapping. The governing equations of the VOF-based multi-phase flow model are

$$\frac{\partial}{\partial t}(\varepsilon\rho) + \nabla\cdot(\varepsilon\rho\mathbf{u}) = 0 \tag{1}$$

$$\frac{\partial}{\partial t}(\varepsilon\rho\mathbf{u}) + \nabla\cdot(\varepsilon\rho\mathbf{u}\mathbf{u}) = \nabla\cdot[\varepsilon(\eta+\eta_t)(\nabla\mathbf{u}+\nabla\mathbf{u}^{\mathbf{T}})] + \varepsilon(\rho\mathbf{g}-\nabla p-\mathbf{R}) \tag{2}$$

where t, ε, $\mathbf{u}$, $\mathbf{g}$, and p are the time, porosity, physical velocity vector, gravitational acceleration, and pressure, respectively. The density (ρ) and viscosity (η) are associated with the local volume fraction of each phase and are obtained by solving the advection equation of the volume fraction

$$\frac{\partial}{\partial t}(\varepsilon\alpha_{\text{water}}) + \nabla\cdot(\varepsilon\alpha_{\text{water}}\mathbf{u}) = 0 \tag{3}$$

$$\frac{\partial}{\partial t}(\varepsilon\alpha_{\text{oil}}) + \nabla \cdot (\varepsilon\alpha_{\text{oil}}\mathbf{u}) = 0 \tag{4}$$

$$\alpha_{\text{air}} = 1 - \alpha_{\text{oil}} - \alpha_{\text{water}} \tag{5}$$

$$\rho = \rho_{\text{oil}}\alpha_{\text{oil}} + \rho_{\text{water}}\alpha_{\text{water}} + \rho_{\text{air}}\alpha_{\text{air}} \tag{6}$$

$$\eta = \eta_{\text{oil}}\alpha_{\text{oil}} + \eta_{\text{water}}\alpha_{\text{water}} + \eta_{\text{air}}\alpha_{\text{air}} \tag{7}$$

where α_{water}, α_{oil}, α_{air} represent the volume fraction of water, oil, and air respectively, while ρ_{water}, ρ_{oil}, ρ_{air} and η_{water}, η_{oil}, η_{air} are the density and viscosity of each phase. In equation (2), **R** is the flow resistance of the fluid passing through the packed bed, expressed by the well-known Ergun equation

$$\mathbf{R} = \frac{\varepsilon}{A}\eta\mathbf{u} + \frac{\varepsilon^2 B}{2}\rho\mathbf{u}|\mathbf{u}| \tag{8}$$

In the equation, A is the permeability of the packed bed and B is the inertial term, given by

$$A = \frac{d_{\text{p}}^2}{150}\frac{\varepsilon^3}{(1-\varepsilon)^2} \tag{9}$$

$$B = \frac{3.5}{d_{\text{p}}}\frac{(1-\varepsilon)}{\varepsilon^3} \tag{10}$$

where d_{p} is the effective particle size. For the main part of the model, i.e., the Hele-Shaw cell, the laminar model is activated: thus, $\eta_{\text{t}} = 0$ in this zone. However, the turbulence model is applied in the outlet channel to gain a more accurate velocity field calculation in this zone since the velocity is considerable. The RNG k-ε turbulence model is used to simulate the mean flow characteristics of the turbulent conditions.

2.3. Model Settings and Model Implementation

The computational domain and boundary conditions are illustrated schematically in Figure 1. The main part, i.e., light blue region, of the model is fully occupied by the particle packed bed except in the cases considering the effect of a coke-free zone. The outlet channel includes four parts and their lengths (l) and radius (r) are also shown schematically in the figure: these roughly correspond to the counterparts in the experimental rig.[26] The inlet (upper) boundary

of the model is a fixed pressure inlet and a pressure boundary condition is also applied to the outlet, which is set as atmospheric pressure. No-slip wall boundary conditions are applied to the sidewalls and bottom. The computational grid is distributed denser near the outlet channel and in the outlet channel (cf. lower panel of Figure 1) to capture the local interface bending behaviors more accurately.

The commercial software ANSYS Fluent 2020 R1 was employed to solve the equations of the CFD model, applying a second-order scheme to discretize the governing equations for a high computation precision. The geometric reconstruction approach was used to describe the l-l and l-g interfaces. Time step and under-relaxation factors were set carefully to achieve a nice balance between the overall convergence and calculation time. The physical properties of the fluids used in the model are listed in **Table. 1**.

Table 1. Physical properties of fluids in the model.

Properties	air	water	oil
Density (kg m^{-3})	1.225	998	855
Dynamic viscosity (Pa s)	1.79×10^{-5}	0.001	0.131

3. Simulation Cases and Model Validation

3.1. Simulation Cases

For stable and efficient BF operation, it is important to keep the liquid levels in the hearth within certain limits. The drainage is influenced by the operation conditions, such as blast pressure, deadman permeability, coke-free zone, and initial accumulated liquids. At the start of tapping, the levels of iron and slag depend on the evolution of the previous tap, the production rates of iron and slag, and the time between the taps. Other factors, such as deadman permeability and coke-free zone, can also affect the drainage significantly. To understand this

interaction of variables, a series of cases were simulated to gain a better understanding of the factors affecting BF hearth drainage.

The main conditions of the simulated cases are listed in **Table 2**, where the first case acts as a base case. The absolute thickness of the oil layer at the start of tapping (i.e., the height difference of the initial two interfaces) is denoted by $h_{\mathrm{oil},0}$, and the initial water-oil interface level with respect to the outlet by $h_{\mathrm{l\text{-}l},0}$ (in **Figure 2**). The variable Δp is the difference between inlet and outlet pressures, while h_{cf} is the height of the coke-free zone, which is a region without a packed bed that starts from the model bottom. Here, the top surface shape of the coke–free zone was for the case of simplicity taken to be flat. The permeability of the packed bed (A) is determined by

$$A = b^2/12 \tag{11}$$

where $b = 2$ mm is the thickness of the Hele-Shaw model used in the experimental work.[12] Thus, the base-case permeability of the CFD model is $A = 0.333 \times 10^{-6}$ m^2.

Table 2. Parameters for the simulation cases, expressing initial oil-layer thickness, water level with respect to the taphole, pressure drop, bed permeability, and height of the coke-free zone (cf. Figure 2). Perturbed parameter values are written in bold.

Case number	$h_{\mathrm{oil},0}$ mm	$h_{\mathrm{l\text{-}l},0}$ mm	Δp bar	$A \times 10^6$ m^2	h_{cf} mm
1	120	0	0.3	0.333	0
2	**100**	0	0.3	0.333	0
3	**140**	0	0.3	0.333	0
4	120	**– 20**	0.3	0.333	0
5	120	**+ 20**	0.3	0.333	0
6	120	0	**0.2**	0.333	0
7	120	0	**0.4**	0.333	0
8	120	0	0.3	**0.083**	0
9	120	0	0.3	**1.332**	0
10	120	0	0.3	0.333	**85**
11	120	0	0.3	0.333	**170**

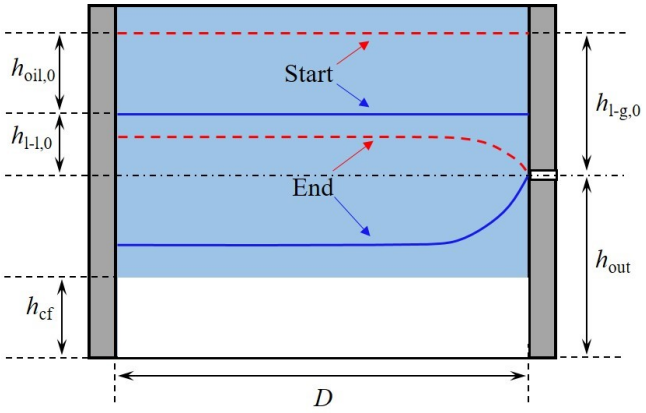

Figure 2. Schematic illustration of the initial and final interface states. Dashed lines: l-g interfaces, Solid lines: l-l interfaces, Light blue area: packed bed zone, White area: coke-free zone.

3.2. Model validation

For the VOF-based model, the mesh resolution is essential for achieving accurate results. Therefore, a grid independence test was first conducted. The tapping time was employed as the key parameter characterizing the hearth drainage to validate the CFD model. For the simulation with the conditions $h_{l\text{-}l,0}$ = 10 mm, $h_{oil,0}$ = 100 mm, Δp = 0.3 bar and μ_{oil} = 0.131 Pa s, which correspond to the base case of the earlier experimental study by the authors (cf. Table 2 of ref. [12]), three grid resolution scales were examined: a coarse scale with 96000 cells, an intermediate scale with 226901 cells, and dense scale with 364987 cells. The tapping time for the three cases was found to be 3.55 s, 3.69 s, and 3.65 s, respectively. As a compromise between computation cost and accuracy, the intermediate scale mesh resolution was selected for the simulations to be presented in what follows.

To verify the model, some cases with different initial oil-layer thicknesses ($h_{oil,0}$) were studied. The simulated results and associated experimental data[12] were collected and are presented in **Figure 3**, which shows an excellent agreement between the experimental and simulated tapping times for the different values of $h_{oil,0}$. Thus, the accuracy of the CFD model is demonstrated.

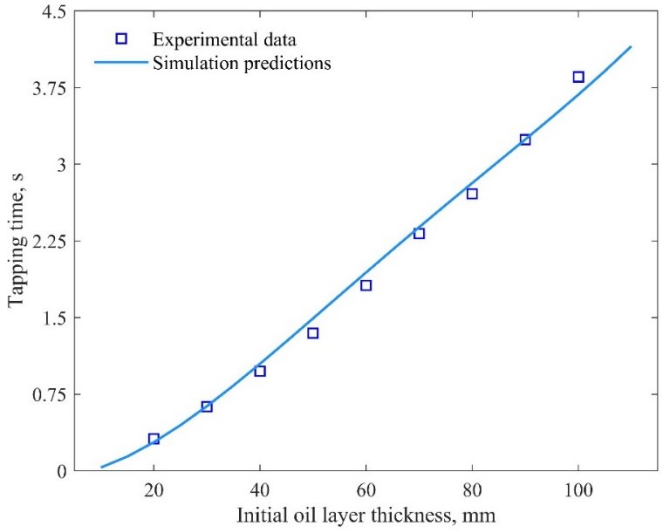

Figure 3. Effect of initial oil-layer thickness on gas break-through (i.e., tapping) time in the experiments (squares) and simulations (line). Conditions: $h_{oil,0}$: 10-110 mm, $h_{l\text{-}l,0}$: +10 mm, Δp: 0.3 bar, A: 0.333×10^{-6} m^2, h_{cf}: 0 mm.

4. Results and Discussion

4.1. Interface level and liquid volume evolution

To investigate and compare the tapping behavior under different conditions, the evolutions of the interface levels and liquid volumes are depicted, both in absolute time and normalized time: the latter is given by t/t_{total}, where t_{total} is the total tapping time.

4.1.1. Effect of initial oil-layer thickness (Cases 1-3)

Cases 1-3 in Table 2 examine the influence of the initial oil-layer thickness on the evolution of the average interface levels, $\bar{h}$, (upper panels) and liquid volumes (lower panels) of **Figure 4**. The left upper panel shows that the average l-g interface levels ($\bar{h}_{l\text{-}g}$, red lines) descend parallelly and linearly with the tapping time for the different initial oil-layer thicknesses. Similar trends are also found in the evolutions of total and oil volume (cf. left lower panel). For the three cases, the average l-l interface level ($\bar{h}_{l\text{-}l}$, blue lines) evolutions are identical, so the three curves fall on each other. Naturally, the same holds for the water volumes. Thus, as expected, the initial thickness of the oil layer does not affect the outflow of the water. To make a

comparison of the average interface levels and liquid volumes at the termination of the drainage, the evolutions are also depicted in normalized time. The right panels illustrate that the end level of the liquid-liquid interface ($\bar{h}_{\text{l-l,end}}$) becomes lower and the end level of the liquid-gas interface ($\bar{h}_{\text{l-g,end}}$) becomes higher as the initial oil-layer thickness increases. The reason is that a higher initial oil-layer thickness extends the tapping time, so more oil and water can be drained, which leads to a lower $\bar{h}_{\text{l-l,end}}$. In addition, the lower water level will increase the oil outflow rate and oil ratio in the outflow (cf. subsection 4.2), generating a larger pressure loss in the bed, so the oil-air interface bends more, causing a higher $\bar{h}_{\text{l-g,end}}$.

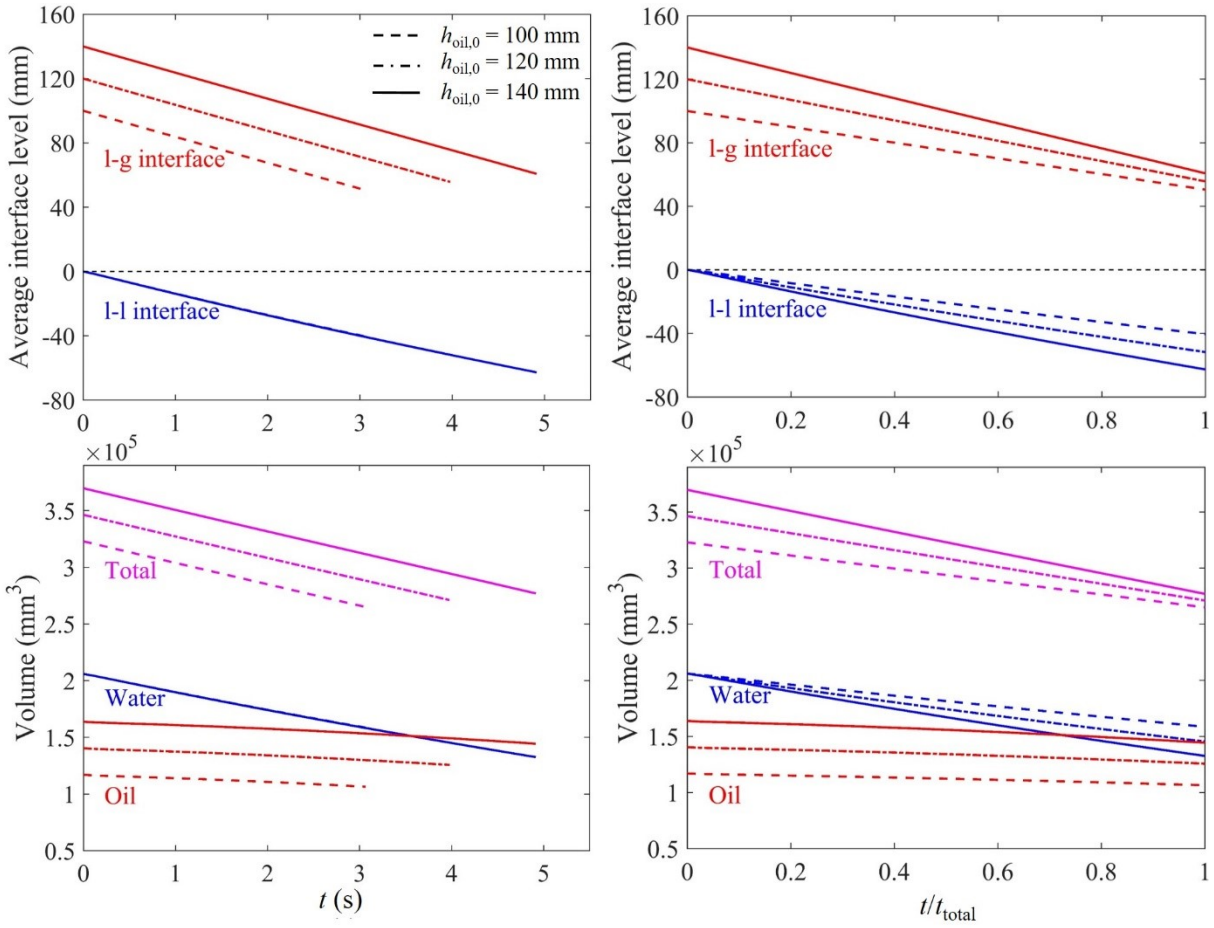

Figure 4. Effect of initial oil-layer thickness in absolute (left panels) and normalized (right panels) time. Upper panels: Evolution of the average interface levels. Lower panels: Evolution of liquid volumes in the model. Conditions: $h_{\text{l-l,0}}$: 0 mm, Δp: 0.3 bar, A: 0.333×10^{-6} m^2, h_{cf}: 0 mm.

4.1.2. Effect of packed bed permeability (Cases 1, 8 and 9)

Figure 5 shows how the liquid levels and volumes evolve for different packed bed permeabilities (0.083×10^{-6} m^2, 0.333×10^{-6} m^2, and 1.332×10^{-6} m^2). The left panels show that a higher bed permeability can increase the tapping time and the oil outflow rate. The reason is that a good bed permeability decreases the pressure drop in the bed (especially for the oil) when the liquids pass through it, which results in a relatively flat l-g interface during the drainage (cf. subsection 4.3): the l-g interface does not bend so much and this extends the tapping time. Thus, a good bed permeability enhances the oil outflow rate.

A higher bed permeability lowers $\bar{h}_{\text{l-g,end}}$ and $\bar{h}_{\text{l-l,end}}$ due to a longer drainage time. This stresses that it is essential to maintain a good coke-bed (deadman) permeability in the BF hearth for gaining lower liquid levels in the hearth at the end of the tapping. Means to keeping the deadman permeability in a good state include a proper control of the blast velocity in the tuyeres, the pulverized coal rate, and charging strong and large coke in the center.

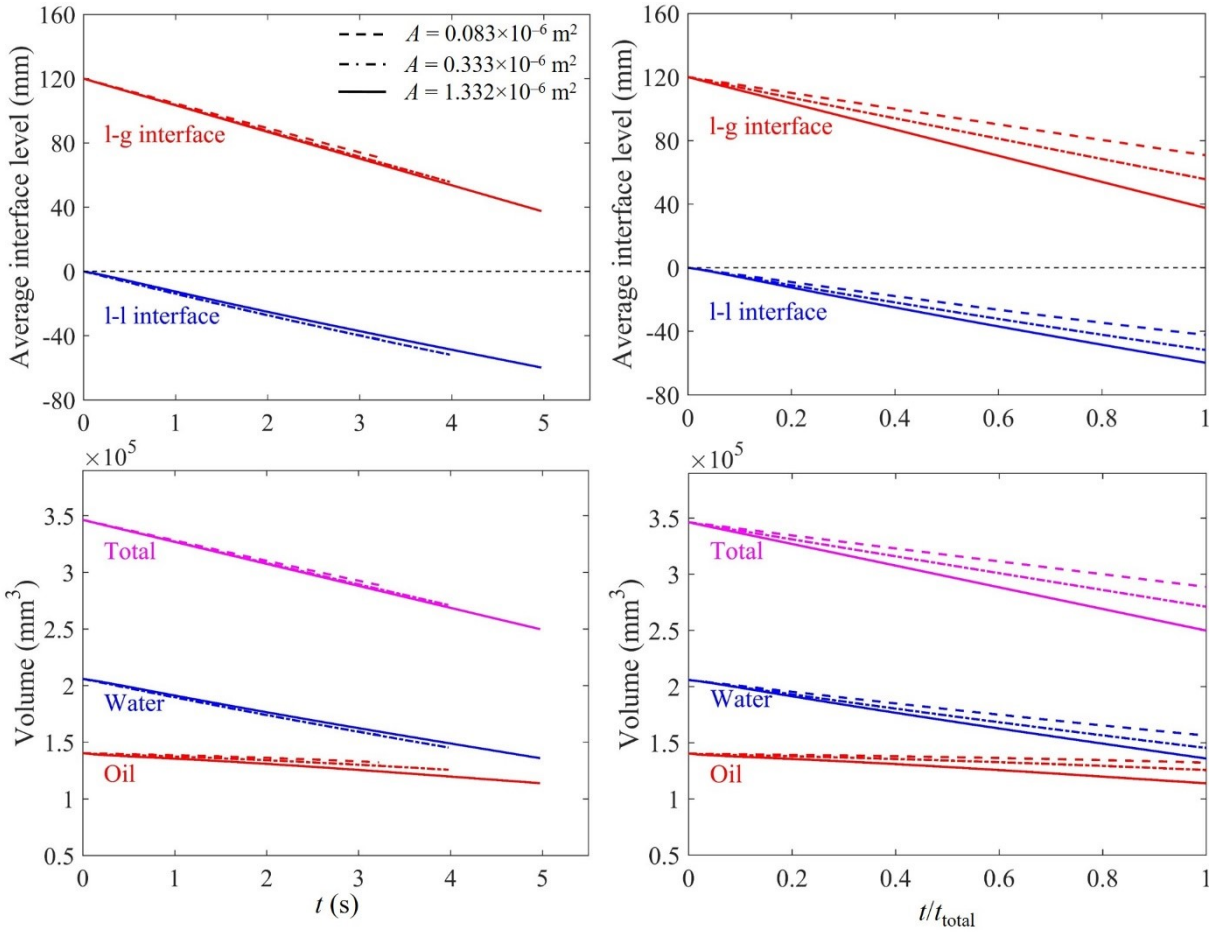

Figure 5. Effect of packed bed permeability in absolute (left panels) and normalized (right panels) time. Upper panels: Evolution of the average interface levels. Lower panels: Evolution of liquid volumes in the model. Conditions: $h_{oil,0}$: 120 mm, $h_{l\text{-}l,0}$: 0 mm, Δp: 0.3 bar, h_{cf}: 0 mm.

4.1.3. Effect of pressure difference (Cases 1, 6 and 7)

The effect of the pressure difference on the evolutions of the liquid levels and volumes is depicted in **Figure 6**. The left panels illustrate that the descent rates of both interfaces increase with the pressure difference in the system. However, a higher pressure difference yields more residual liquids at the end of tapping, which is seen more clearly in the right panels that depict the evolution in normalized time. Thus, a better drainage could be obtained by employing a smaller blast pressure in the BF, but the benefits of a higher blast pressure (e.g., lower linear gas velocity and suppression of gasification reactions) are usually considered to be stronger in the practical operation of the BF.

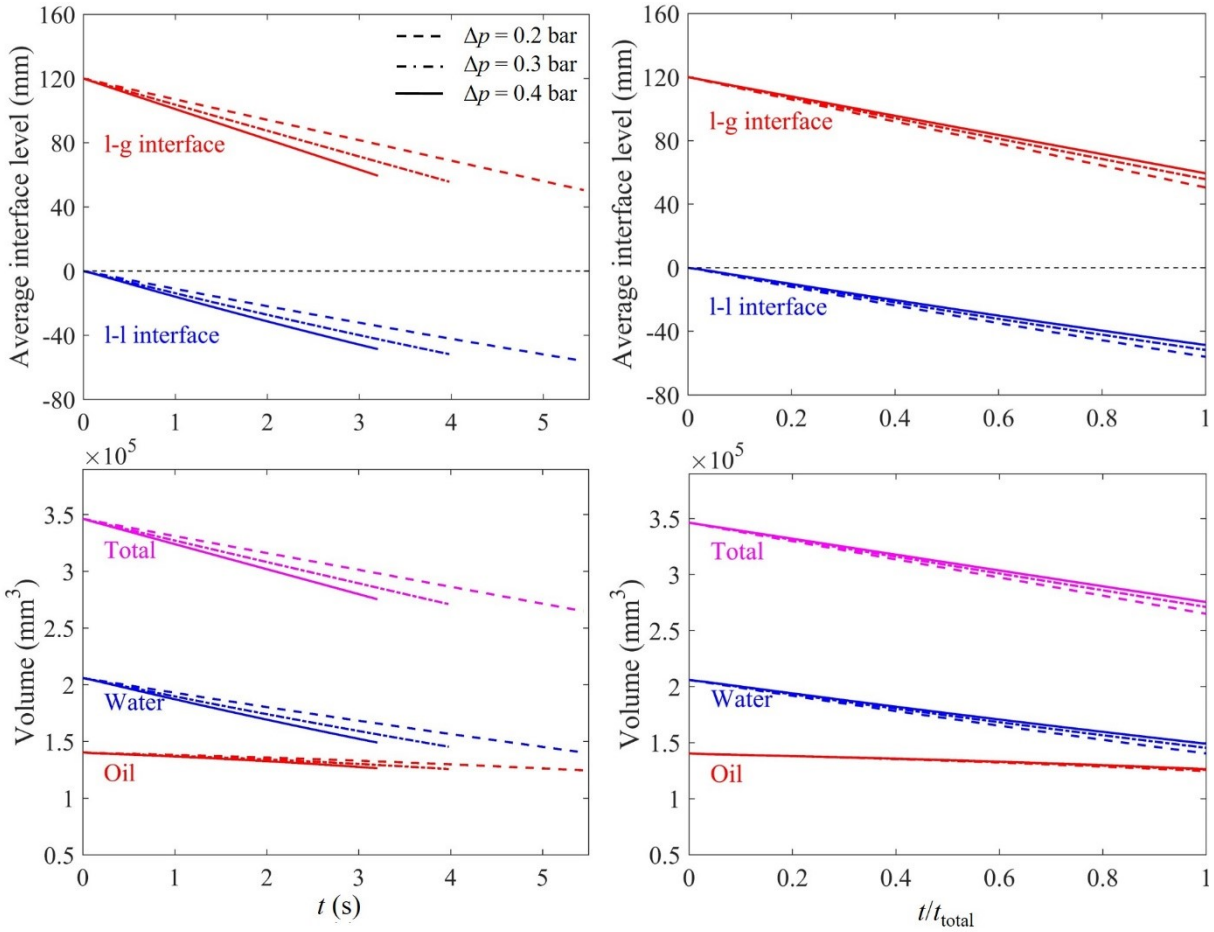

Figure 6. Effect of pressure difference in absolute (left panels) and normalized (right panels) time. Upper panels: Evolution of the average interface levels. Lower panels: Evolution of liquid volumes in the model. Conditions: $h_{oil,0}$: 120 mm, $h_{l\text{-}l,0}$: 0 mm, A: 0.333×10^{-6} m^2, h_{cf}: 0 mm.

4.1.4. Effect of initial l–l interface level (Cases 1, 4 and 5)

The role of the initial l-l interface level on the evolutions of the liquid levels and volumes is illustrated in **Figure 7**. The initial level is seen not to affect the end levels of oil and water. The main influence of the initial l-l interface level is on the draining time and the delay before the second liquid phase starts flowing out. For the industrial counterpart, the initial l-l interface level strongly affects the initial part of the tapping patterns, i.e., whether only iron, iron and slag, or only slag will be drained first.

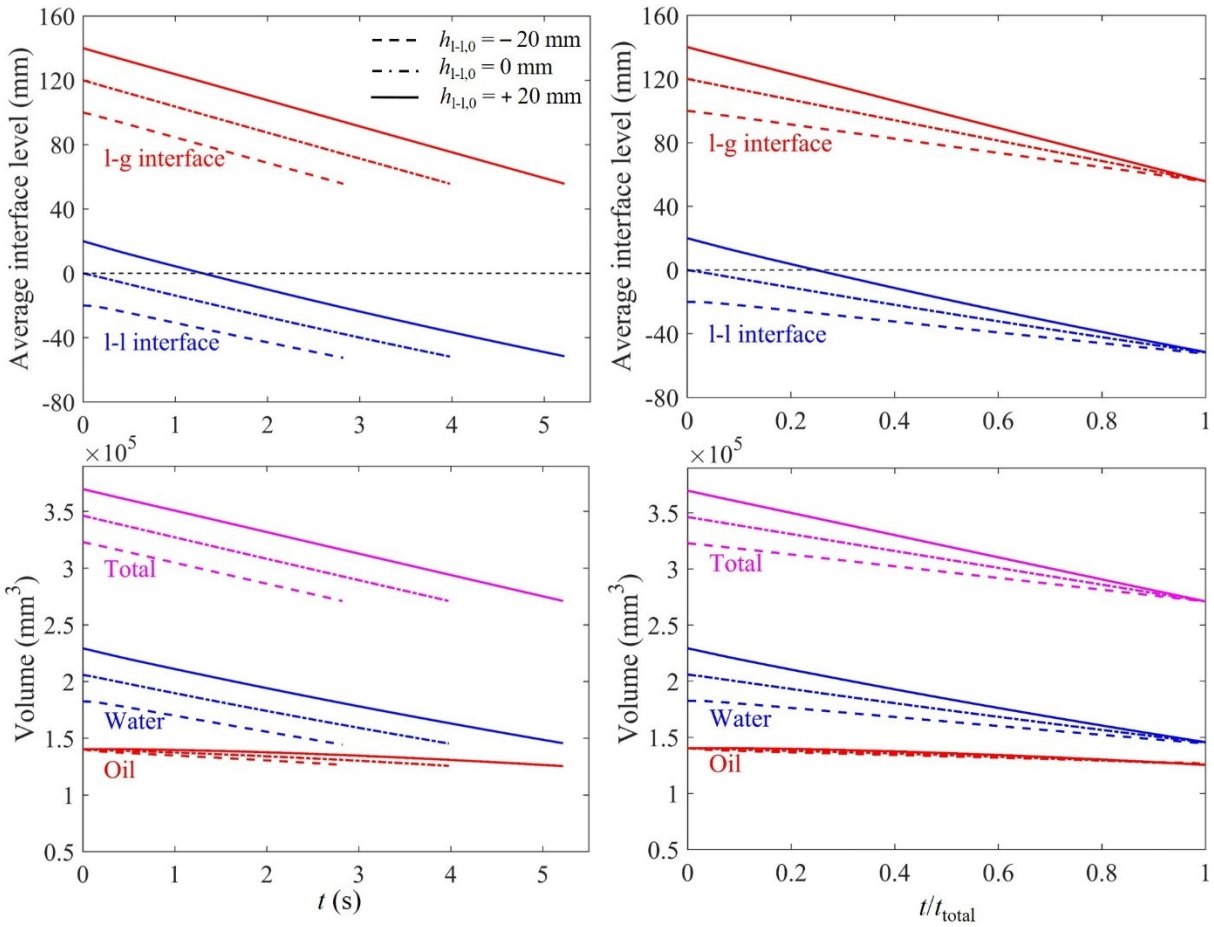

Figure 7. Effect of initial l-l interface level in absolute (left panels) and normalized (right panels) time. Upper panels: Evolution of the average interface levels. Lower panels: Evolution of liquid volumes in the model. Conditions: $h_{oil,0}$: 120 mm, Δp: 0.3 bar, A: 0.333×10^{-6} m^2, h_{cf}: 0 mm.

4.1.5. Effect of coke-free zone (Cases 1, 10 and 11)

Figure 8 depicts the dependence of the liquid levels and volumes on the height of the coke-free zone (0 mm, 85 mm, and 170 mm) in the bottom of the system. The left panels illustrate that the coke-free zone has practically no effect on the oil and water drainage if it is not high enough to allow the oil to flow through it during the tapping. These results are identical with the findings by He et al.[11] However, for the case where the coke-free zone extends close to the outlet level, it is possible to drain out the oil through this zone, which prolongs the draining time. The reason for this is that the lower pressure drop in the oil phase decreases the bending degree of the l-g interface. The small oil flow resistance results in a much higher oil outflow rate (cf. subsection 4.2). Thus, oil becomes the dominating outflow, yielding more residual

water and less residual oil at the end of tapping (cf. right panels of Figure 8). The higher water-oil end level is due to the lower pressure drop in the oil phase. Hence, the pressure in front of the taphole does not decrease so much and less water can be "pumped up".

In the BF hearth, the formation of coke-free zone is due to deadman floating. The deadman state is a result of a balance of the forces acting upon it. Because these forces vary with the conditions, and in particular with the wear of the hearth bottom, the deadman may float and sit during different phases of the campaign. Even though some investigators have claimed that the lower end of the deadman may (locally) extend to levels to or above the taphole,[10,27] this state is still considered to be rather rare.

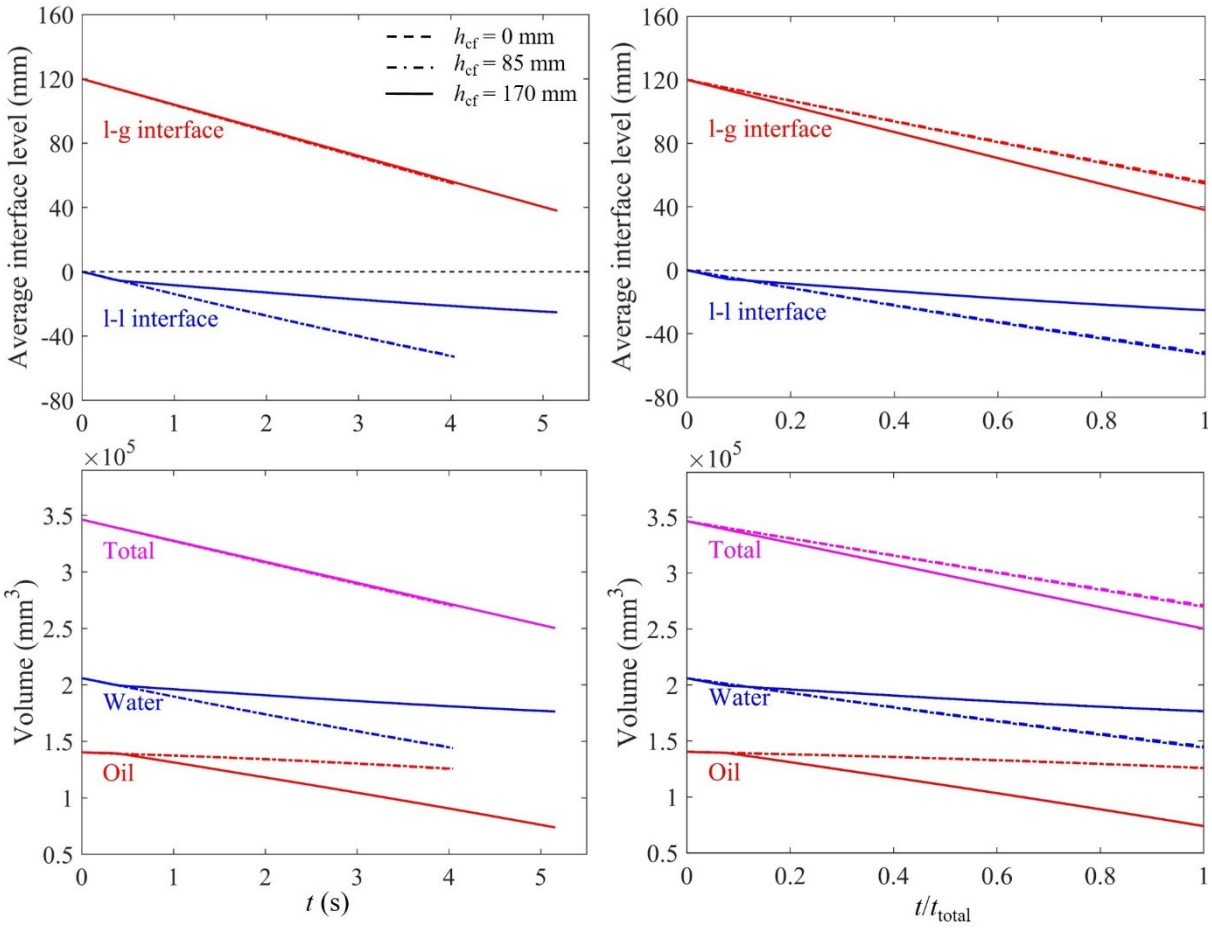

Figure 8. Effect of the coke-free zone in absolute (left panels) and normalized (right panels) time. Upper panels: Evolution of the average interface levels. Lower panels: Evolution of liquid volumes in the model. Conditions: $h_{oil,0}$: 120 mm, $h_{l\text{-}l,0}$: 0 mm, Δp: 0.3 bar, A: 0.333×10^{-6} m^2.

4.2. Outflow rate and oil ratio

The outflow rates of liquids and their ratio are also important factors characterizing the hearth drainage, so these were also analyzed for all the cases studies. The oil ratio is here defined as the volume flowrate of oil divided by the volume flowrate of water. Like for the liquid levels and volumes, the variables are next studied in both absolute and normalized time.

4.2.1. Effect of initial oil-layer thickness (Cases 1-3)

The effect of the initial oil-layer thickness on the outflow rates and oil ratio is depicted in **Figure 9**. The upper panels illustrate that the water outflow rate at the termination of the drainage slightly decreases with the initial oil-layer thickness, while the oil outflow rate shows an opposite trend, which naturally yields a higher oil ratio shown in the lower panels. As noted in subsection 4.1.1, the reason is that a lower l-l interface level makes it is more difficult to drain water at the final parts of the tapping.

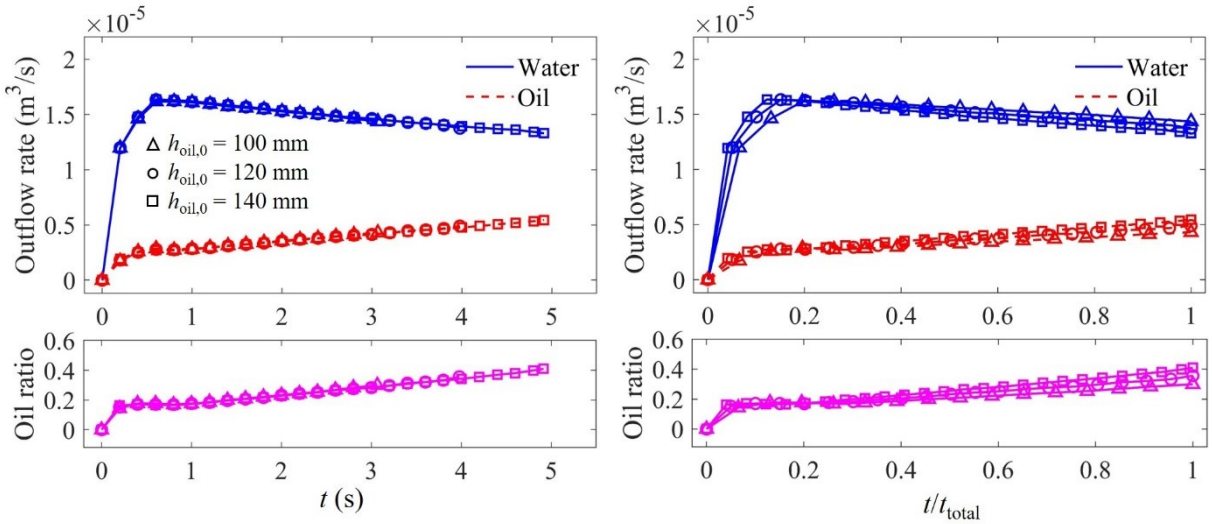

Figure 9. Effect of initial oil-layer thickness in absolute (left panels) and normalized (right panels) time. Upper panels: Evolution of the outflow rates. Lower panels: Evolution of ratio of oil and water. Conditions: $h_{l\text{-}l,0}$: 0 mm, Δp: 0.3 bar, A: 0.333×10^{-6} m^2, h_{cf}: 0 mm.

4.2.2. Effect of packed bed permeability (Cases 1, 8 and 9)

Figure 10 depicts the evolutions of outflow rates and oil ratio for the cases with different bed permeabilities (0.083×10^{-6} m^2, 0.333×10^{-6} m^2, and 1.332×10^{-6} m^2). A higher permeability

enhances mainly the oil outflow rate, as oil is the more viscous phase, as seen in the upper panels. Naturally, a bigger oil outflow rate also leads to a bigger oil ratio, as depicted in the lower panels.

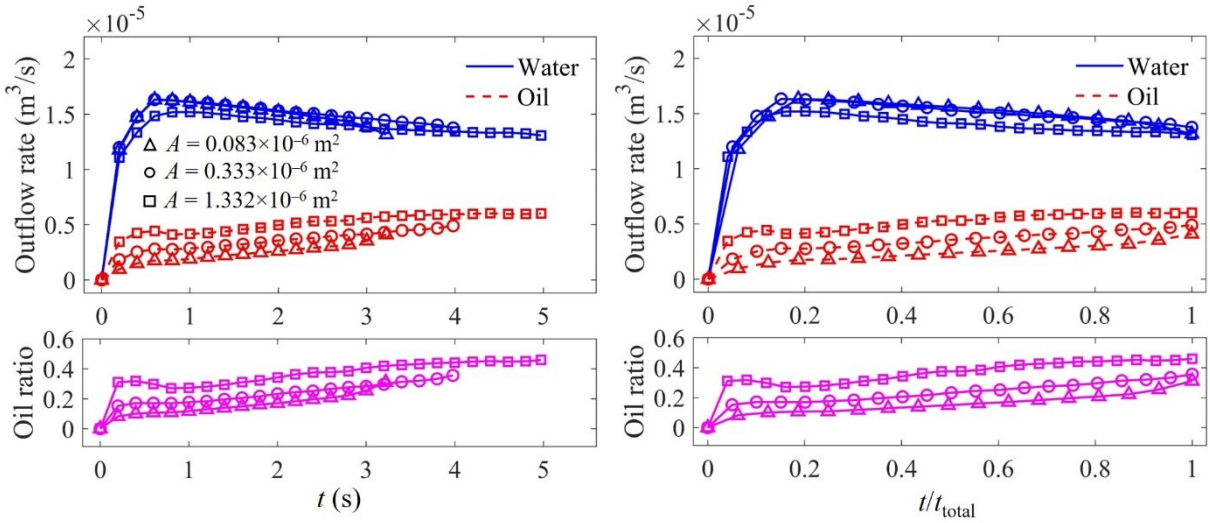

Figure 10. Effect of packed bed permeability in absolute (left panels) and normalized (right panels) time. Upper panels: Evolution of the outflow rates. Lower panels: Evolution of ratio of oil and water. Conditions: $h_{oil,0}$: 120 mm, $h_{l\text{-}l,0}$: 0 mm, Δp: 0.3 bar, h_{cf}: 0 mm.

4.2.3. Effect of pressure difference (Cases 1, 6 and 7)

The effect of pressure difference on the outflow rates, depicted in the upper panels of **Figure 11**, illustrates that both oil and water outflow rates increase significantly with the pressure difference, because it is the main driving force for the drainage. The lower panels show that the pressure difference has practically no effect on the oil ratio in normalized time.

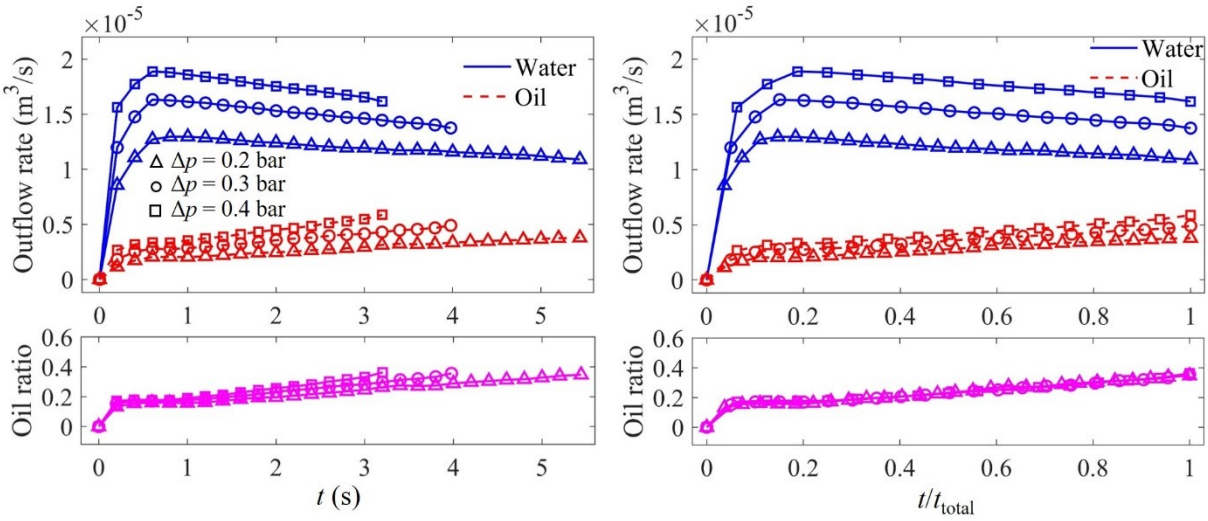

Figure 11. Effect of pressure difference in absolute (left panels) and normalized (right panels) time. Upper panels: Evolution of the outflow rates. Lower panels: Evolution of ratio of oil and water. Conditions: $h_{oil,0}$: 120 mm, $h_{l\text{-}l,0}$: 0 mm, A: 0.333×10^{-6} m^2, h_{cf}: 0 mm.

4.2.4. Effect of initial l–l interface level (Cases 1, 4 and 5)

Figure 12 depicts that an increased initial l-l interface level clearly affects the outflow pattern in the first part of the tapping. For the case with a high initial l-l interface level (+ 20 mm), water-only flow occurs at the start of the drainage, while for the case with a low initial level (– 20 m), oil-only flow occurs first, yielding a clear spike in the oil ratio. The results show that the "competition" of the two phases in the drainage is largely governed by the internal liquid levels. As time elapses, the outflow rates and oil ratio for the three cases are seen to converge in normalized time.

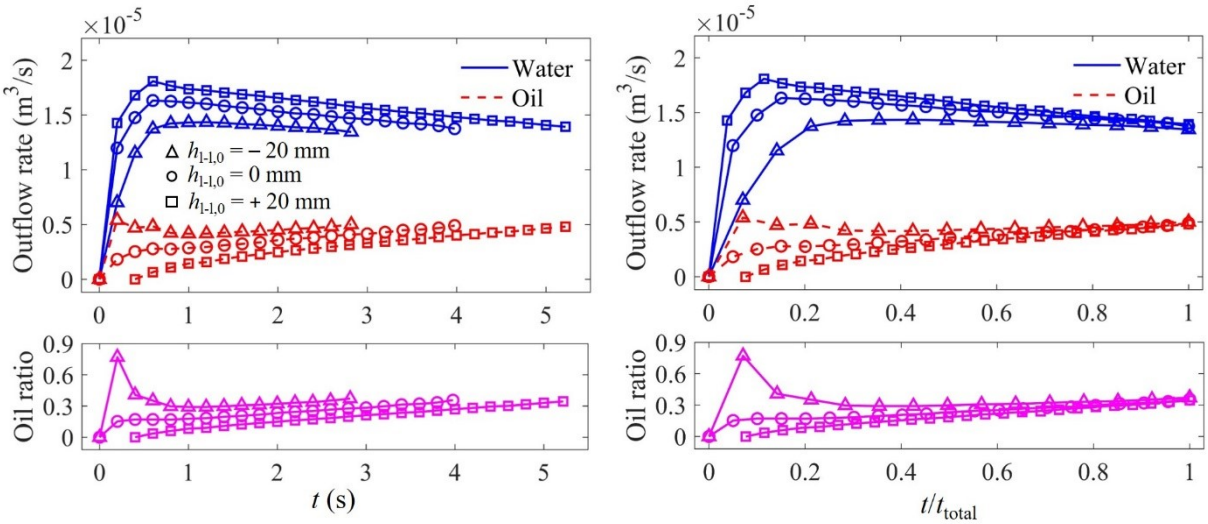

Figure 12. Effect of initial l-l interface level in absolute (left panels) and normalized (right panels) time.

Upper panels: Evolution of the outflow rates. Lower panels: Evolution of ratio of oil and water. Conditions: $h_{oil,0}$: 120 mm, Δp: 0.3 bar, A: 0.333×10^{-6} m^2, h_{cf}: 0 mm.

4.2.5. Effect of coke-free zone (Cases 1, 10 and 11)

Figure 13, which depicts the influence of a coke-free zone on the evolution of outflow, shows that there is no effect if the coke-free zone does not extend (close) to the outlet. However, if it does, the oil outflow rate increases dramatically and oil is the dominating phase that drains (for reasons already discussed in subsection 4.1.5).

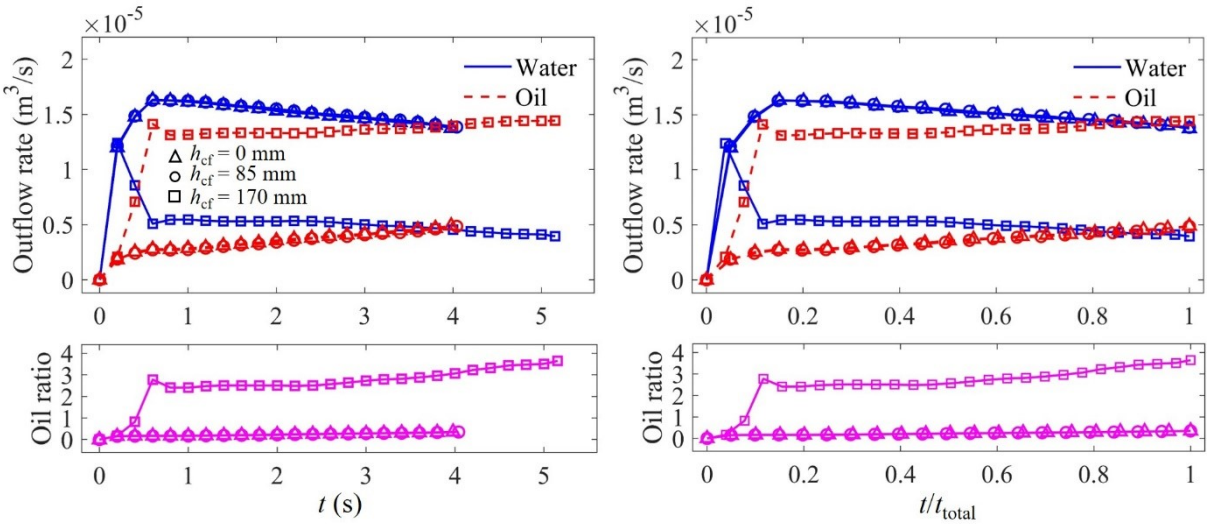

Figure 13. Effect of coke-free zone in absolute (left panels) and normalized (right panels) time. Upper panels: Evolution of the outflow rates. Lower panels: Evolution of ratio of oil and water. Conditions: $h_{oil,0}$: 120 mm, $h_{l\text{-}l,0}$: 0 mm, Δp: 0.3 bar, A: 0.333×10^{-6} m^2.

4.3 Interface angle

During hearth drainage, the l-l and l-g interface bendings change continuously and are related to furnace operation conditions (e.g., blast pressure, deadman permeability, etc). As mentioned above, the local l-g interface bending has a strong effect on the tapping time. Therefore, a quantitative analysis of the interface bending during the tapping was undertaken by studying a local region near the outlet channel in detail (cf. **Figure 14a)**.

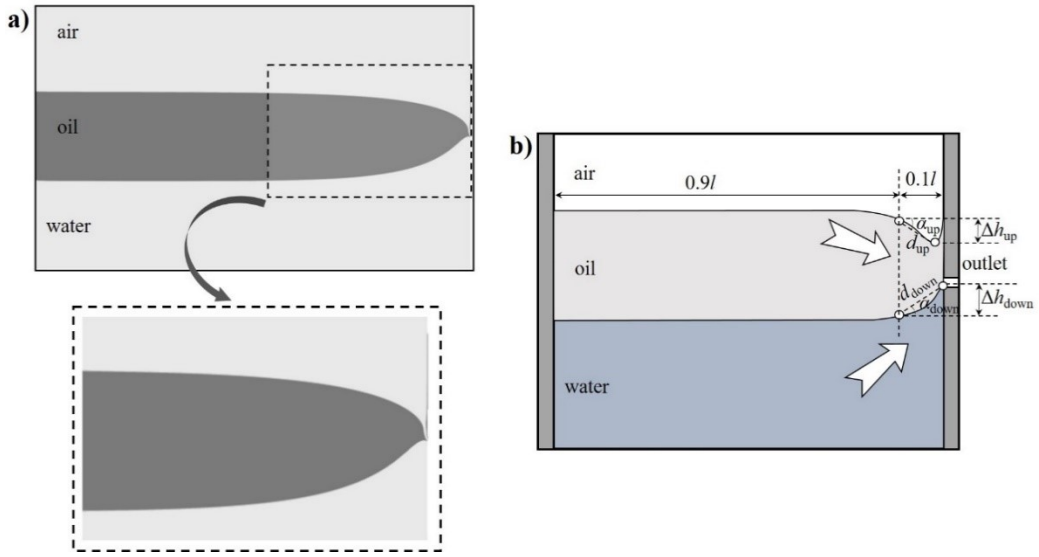

Figure 14. a) Locally extracted area in the model for the determination of the bending angle. b) Interface angles and quantities used to determine them.

Two interface parameters, i.e., the l-g interface angle, α_{up}, and l–l interface angle, α_{down}, are introduced to quantify the interface bending degree. The l-g interface angle depends on the locations of the lowest point and a reference point on the l-g interface, while for the l-l interface angle, the reference point and highest point on the l-l interface are used. The reference points are here chosen as the intersection points of the two interfaces and a vertical line which is placed at a distance of one-tenth of the width (l) of the model from the outlet (cf. Figure 14b). The angles are calculated by

$$\alpha_{\mathrm{up}} = \arcsin\left(\frac{\Delta h_{\mathrm{up}}}{d_{\mathrm{up}}}\right) \tag{12}$$

$$\alpha_{\mathrm{down}} = \arcsin\left(\frac{\Delta h_{\mathrm{down}}}{d_{\mathrm{down}}}\right) \tag{13}$$

where Δh_{up} and d_{up} are the vertical and total distances between the lowest point (on the l-g interface) and the reference point of the interface, respectively, while d_{down} and Δh_{down} are the corresponding distances between the highest point (on the l–l interface) and the reference point of the interface.

4.3.1. Effect of initial oil-layer thickness (Cases 1-3)

The influence of the initial oil-layer thickness is examined first. The interface angles of Cases 1-3 are shown in **Figure 15a**: the l-l interface angle increases with the oil-layer thickness because more oil initially yields a longer tapping time, which makes the water level descend deeper below the outlet. For the l-g interface angle, the effect of the initial oil-layer thickness is insignificant.

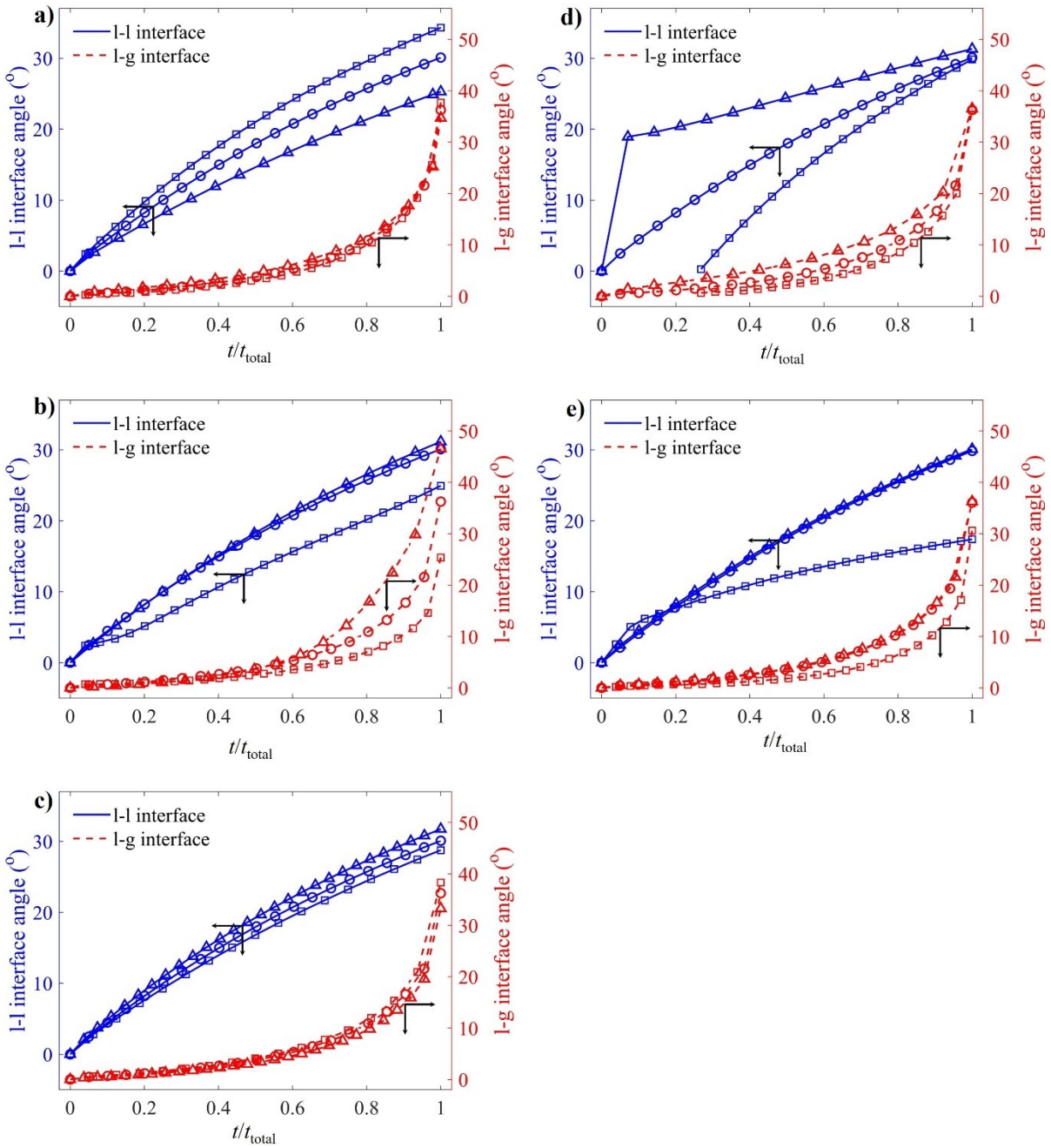

Figure 15. Effect of a) initial oil-layer thickness, b) packed bed permeability, c) pressure difference, d)

initial l-l interface level, and e) coke-free zone on the bending of the l-l and l-g interfaces during the tapping. The studied variable increases when going from triangles, through circles to squares. The conditions are reported in Table 2.

4.3.2. Effect of packed bed permeability (Cases 1, 8 and 9)

The effect of the bed permeability on the interface bending is shown in **Figure 16a**, which depicts the results for the studied bed permeabilities (top row: 0.083×10^{-6} m^2, middle row: 0.333×10^{-6} m^2, bottom row: 1.332×10^{-6} m^2) for three different times distributed uniformly over the drainage duration (t/t_{total} = 1/3, 2/3 and 1). The corresponding interface angle evolutions are depicted in **Figure 15b**. They illustrate that an increased bed permeability substantially decreases the bending degree of both interfaces, and especially that of the l-g interface. Viscous fingering[7] of the l-g interface is observed for the case with a low bed permeability (cf. rightmost panel in the top row). This effect can shorten the tapping time dramatically, which stresses the importance of maintaining a good hearth permeability.

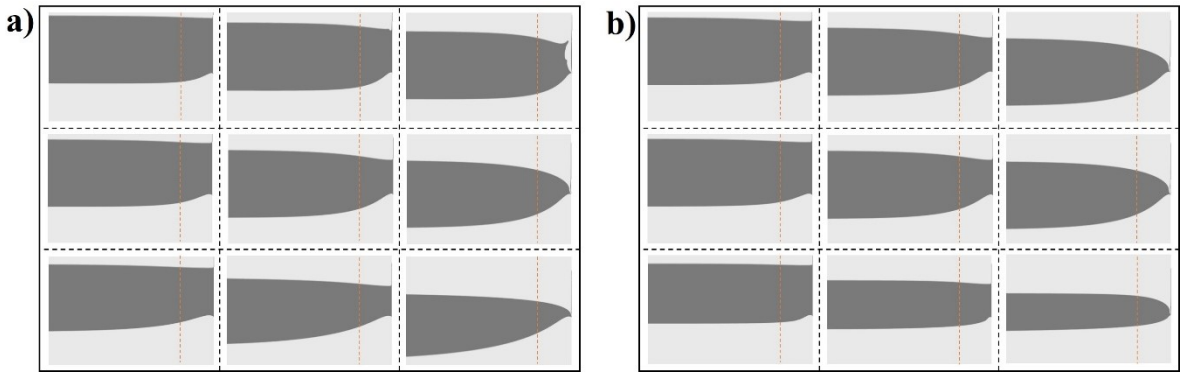

Figure 16. State after one third (leftmost panels), two thirds (center panels), and end (rightmost panels) of the tapping process for an initial oil-layer thickness of 120 mm, initial l-l interface level of 0 mm, and pressure difference of 0.3 bar. a) Effect of packed bed permeability (top row: 0.083×10^{-6} m^2, middle row: 0.333×10^{-6} m^2, bottom row: 1.332×10^{-6} m^2) for a bed without a coke-free zone. b) Effect of coke-free zone height (top row: 0 mm, middle row: 85 mm, bottom row: 170 mm) for a bed with a permeability of 0.333×10^{-6} m^2.

4.3.3. Effect of pressure difference (Cases 1, 6 and 7)

The role of the pressure difference, illustrated in **Figure 15c**, shows that the l-g interface bending increases with the pressure difference, while the l-l interface shows an opposite trend.

The former is attributed to a bigger pressure gradient in the oil and the latter is caused by the large quantity of residual water because of the shorter tapping time.

4.3.4. Effect of initial l-l interface level (Cases 1, 4 and 5)

Figure 15d shows how the initial l-l interface level affects the interface bending. The l-g interface bends more for the case with a lower initial l-l interface level, and a similar but stronger trend is seen for the l-l interface, but the final bending degrees are only marginally affected by the initial l-l interface level. This implicitly implies that the average interfaces levels at the end of the drainage become identical, as also seen in Fig. 6.

4.3.5. Effect of coke-free zone (Cases 1, 10 and 11)

Figures 15e and **16b** show how the interface angles change with the height of the coke-free zone. The effect is very small if the coke-free zone is not high enough to affect the oil flow, but when oil can flow out through the coke-free zone, the interfaces bend clearly less. This shows the important role of the pressure drop in the more viscous liquid phase in front of the outlet for the evolution of the liquid levels and interface bending.[15]

4.4 Comparison with findings from pilot-scale experiments and BF drainage

Finally, it may be instructive to compare some of the results of the CFD model with the findings of its experimental counterpart and with measurements from an industrial blast furnace. Results from the experimental Hele-Shaw rig have been presented earlier by Liu et al.[12,25,26]

The upper panels of **Figure 17** show a comparison between the simulated liquid levels (left), reproduced from Fig. 6 of the present paper, and the experimental results (right) from the Hele-Shaw model.[26] It should be noted that the experimental conditions differed slightly from the simulated ones with respect to initial oil-level thickness (120 mm in the present study, 100 mm in the experiments) and initial liquid-liquid interface level (0 mm in the present study, 10 mm in the experiments). Despite some nonlinearity in the experimental results, the findings are seen to agree quite well. The lower panels of the figure depict the simulated outflow rate (taken from

Fig. 11, but expressed in l/min) and the experimental results. These subfigures again show striking similarities and also reveals the reason for the nonlinear evolution of the liquid levels in time: in the experimental rig, the outflow rates, and particularly that of water, decrease at the final parts of the drainage. As mentioned in the Appendix of the paper by Liu et al.[26] this may be ascribed to the complex two-phase flow of the viscous oil together with the non-viscous water in the outflow pipe and hose segments.

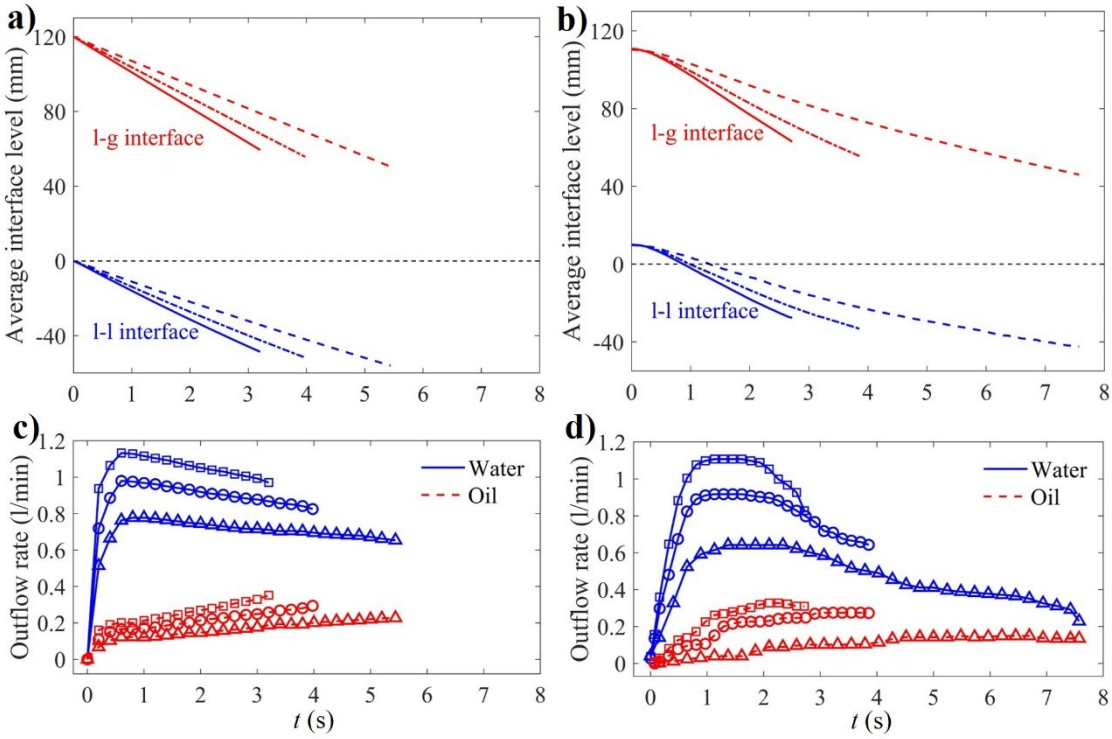

Figure 17. Comparison of simulations and experiments studying the effect of the pressure difference on the liquid levels and outflow rates. a) CFD results reproduced from Fig. 6. b) Experimental results reproduced from Fig. 5 (cf. ref. [26]). c) CFD results reproduced from Fig. 11. d) Experimental results reproduced from Fig. 9 (cf. ref. [26]).

A comparison of the simulated (Figure 18a) and experimental (Figure 18b) effect of the initial oil-layer thickness on the interface profiles at three different times (t/t_{total} = 1/3, 2/3 and 1) shows that an overall agreement between the interface profiles. Figure 18c, which depicts the experimental (dashed lines) and simulated (solid lines) end profiles for the case with $h_{oil,0}$ = 100 mm demonstrate that the simulation model has the ability to describe the interface shape and

bending accurately (even though its tap end has occurred slightly before that of the experimental counterpart).

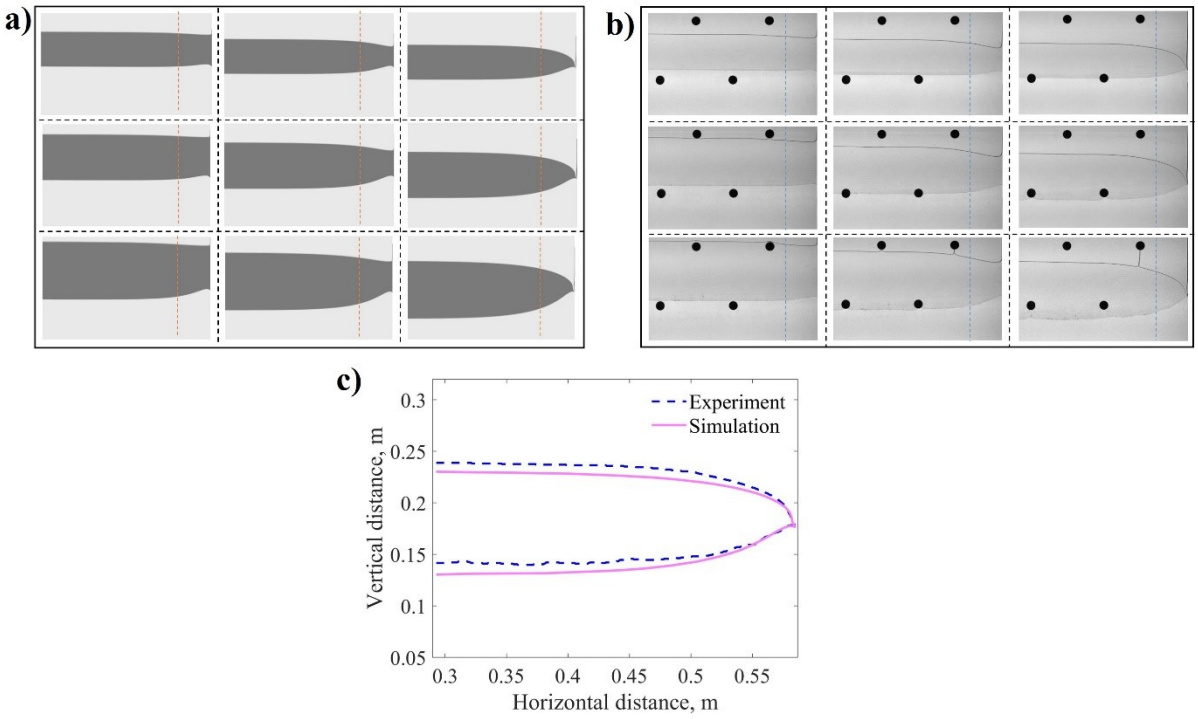

Figure 18. Comparison of simulations and experiments studying the effect of the initial oil layer thickness on the interface bending. a) CFD results. b) Experimental results reproduced from Fig. 14 (cf. ref. [26]). State after one third (leftmost panels), two thirds (center panels), and end (rightmost panels) of the tapping process for an $h_{\text{l-l},0} = 10$ mm, $\Delta p = 0.3$ bar, $h_{\text{cf}} = 0$ mm, $A = 0.333\times10^{-6}$ m^2, $h_{\text{oil},0} = 60$ mm (top row), 80 mm (middle row), 100 mm (bottom row). c) Detailed comparsion of the interfaces at the end state of one case.

As for a comparison between the findings of the CFD model study and observations in the practical operation of the blast furnace, results from a large BF studied by Roche et al.[15] will be used. Under the assumptions that the CFD model describes a quasi-stationary state, where the liquids drained should be balanced by the liquids produced and that the taphole is plugged for a very short time, the ratio between the oil outflow and inflow rates was calculated and depicted for two of the simulated cases. The first is the case with a high bed permeability ($A = 1.332\times10^{-6}$ m^2 studied in Fig. 10) and the second the case with an initial l-l interface below the outlet ($h_{\text{l-l},0} = -20$ mm studied in Fig. 12). The normalized oil outflows, which have been depicted by solid and dashed lines in **Figure 19a**, respectively, show a characteristic pattern

first exhibiting a local maximum soon after the tapping has commenced, followed by a decrease to yield a local minimum and finally a gradual increase. The patterns are more pronounced for the second case, where the system initially drains only oil. Figure 19c depicts the measured (normalized) outflow ratios of slag (blue) and iron (red) for a tap (#224) from the reference BF with slag-only flow in the beginning (taken from Fig. 15 of ref. 15). The normalized slag outflow is seen to qualitatively agree with the normalized oil outflow for the simulated case with $h_{l\text{-}l,0} = -20$ mm (dashed line in Figure 19a). The gradually increasing outflow of iron in the beginning of the tap is also seen to resemble the pattern shown by water in the top right panel of Figure 12. Figure 19b (taken from Fig. 16 of ref. 15) shows the normalized outflows for another tap (#338) of the same BF, where iron and slag start draining practically simultaneously. As seen in Figure 19d, which presents the results of the pressure-balance based model developed by Roche et al.[15] a high porosity (ε) of the deadman can explain the evolution of the slag ratio during the tap. This agrees well with the evolution of the normalized oil outflow of the present CFD model for the case with a high bed permeability (solid line in Figure 19a). Finally, it should be noted that the outflows of iron and slag in the BF increase with the tapping time due to taphole erosion, which was not considered in the CFD model.

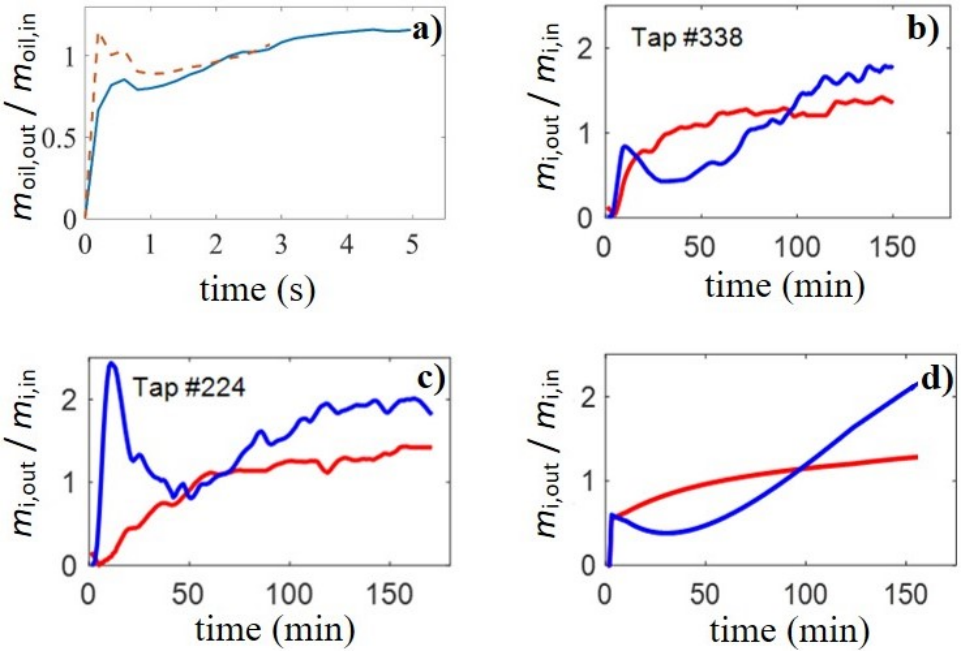

Figure 19. Normalized outflow rate of oil or slag, defined as the outflow rate divided by the production rate. a) Normalized oil outflow for the case of high bed permeability (solid line, cf. Fig. 10) and low initial liquid-liquid interface (dashed line, cf. Fig. 12). b and c) Normalized outflows of slag (blue) and iron (red) for two taps in a large blast furnace (cf. Fig. 15 and Fig. 16 of ref. 15). d) Normalized outflows predicted by model developed by Roche et al.[15] for a high coke-bed permeability.

A way to correlate the simulation results with the findings in the blast furnace and with experimental drainage is through dimensionless analysis. As the amount of residual slag is of primary concern in the industrial system, Zulli[4] has introduced an adjusted dimensionless flow-out coefficient (F_L) which considers the coke-free zone, defined as

$$F_\mathrm{L} = \frac{U_0}{K}\left(\frac{D}{h_{\mathrm{l-g},0}}\right)^{1.94}\left(\frac{h_\mathrm{out} - h_\mathrm{cf}}{h_\mathrm{out}}\right)^{0.5} \tag{14}$$

and demonstrated its relation with the residual ratio of the more viscous phase,

$$\alpha = \frac{V_\mathrm{end}}{V_0} \tag{15}$$

In these expressions, D is the width of the bed (cf. Figure 2), K is the hydraulic conductivity of the bed for oil flow, U_0 is the superficial velocity, $h_{\mathrm{l\text{-}g},0}$ is the initial l-g interface level above the outlet (cf. Fig. 2), h_out is the outlet level (Fig. 2), V_end is the residual volume of the more viscous phase above the outlet at the end of tapping, and V_0 is the initial volume of the more viscous phase above the outlet at the start of drainage.

Figure 20 presents the relation between the flow-out coefficient and the residual oil ratio of the simulation cases in the present study, numbered as in Table 2, showing a clear S-shaped relation between the two variables. While the residual oil ratio increases linearly at intermediate values of F_L, the ratio levels off for higher values of F_L, in agreement with findings of earlier studies.[2,4,12] The moderate changes of the residual oil ratio can be explained by the fact that a thick initial oil layer gives time for the water to descend well below the outlet, thus leaving more residual oil in the system in the end, while the opposite holds true for the case with a thin initial oil layer. The extreme points corresponding to the lowest residual oil ratios arise for the cases where the bed permeability was high (Case 9) or the coke-free zone extended almost to the outlet (Case 11), while the highest residual oil ratio was obtained for the case with the lowest bed permeability (Case 8).

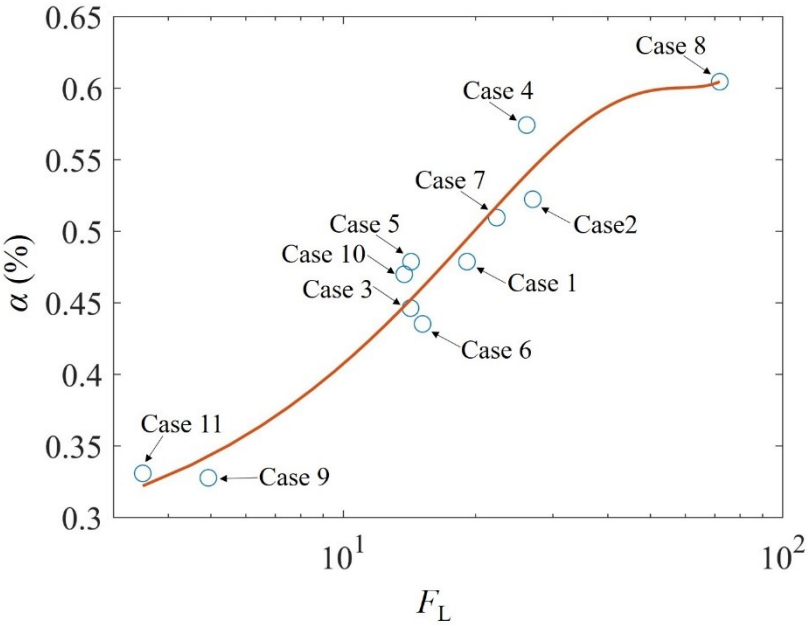

Figure 20. Correlation between the residual oil ratio and flow-out coefficient based on the simulation experiments in the present work.

5. Discussion and Conclusions

A CFD model has been developed to simulate the tapping of two immiscible liquids in an experimental 2D Hele-Shaw model. The model has been applied as a complement to the experimental counterpart to gain a better understanding of the drainage of the blast furnace hearth and how the operation conditions affect the liquid levels and outflows of iron and slag. A series of cases have been simulated with the CFD model, partly reproducing drainage results of oil and water in an experimental Hele-Shaw rig. The CFD model was validated by a comparison with the experimental data showing results in general agreement with the empirical findings. The validated model was employed to study the effect of some key factors on the evolution of average liquid-gas and liquid-liquid interface levels, liquid volumes, outflow rates, oil ratio, as well as interface angles.

Based on the simulation results, the main conclusions can be condensed as:

1) The residual water volume decreases with the initial oil-layer thickness, but the residual oil volume rises. An increased initial oil-layer thickness also decreases the water outflow rate and increases the oil ratio near the end of the tapping.
2) Employing a higher bed permeability, the end interface levels, residual liquid volumes, and bending of both interfaces decrease. The oil outflow rate and oil ratio are also strongly enhanced by the bed permeability, while the water outflow rate decreases slightly. This shows the important role of a good coke-bed permeability for an efficient slag drainage in the blast furnace.
3) A higher pressure difference increases the final interface levels, residual liquid volumes, outflow rates, and the liquid-gas interface angle. The liquid–liquid interface angle and tapping time decrease with the pressure difference in the system. This highlights the role of well-mastered outflow rates to avoid excessive bending of the slag phase at the later parts of the tappings.
4) The initial liquid–liquid interface level mainly affects the tapping time, and yields almost identical interface levels, liquid volumes, outflow rates, oil ratio, and interface angles at the termination of the drainage. Thus, the residual slag ratio is not crucially dependent of the iron level in the blast furnace hearth at tap start. If the liquid-liquid interface level is below the outlet, the oil flow shows a maximum in the beginning of the drainage, in agreement with findings concerning the slag outflow in the industrial system.
5) A low coke-free zone does not affect the drainage, but if the zone extends close to the outlet, much more oil and less water can be drained.

These findings generally agree with earlier findings from the experimental and numerical models and also with the practical observations for the real blast furnace drainage. Future work will focus on extending the model to simulate quasi-stationary operation with production of

liquids and intermittent drainage from one outlet, or alternating drainage from two outlets, which better corresponds to the true operation of the blast furnace hearth.

Acknowledgments

This work was carried out with support from the European Union's Research Fund for Coal and Steel (RFCS) research program under *grant agreement* no. 847332 and from the Åbo Akademi Foundation. This funding is gratefully acknowledged. One coauthor (LS) also wishes to thank the National Natural Science Foundation of China (Grant 51604068) for providing financial support for this work.

Conflicts of Interest: The authors declare no conflict of interest.

References

[1] M. Geerdes, H. Toxopeus, C. Van Der Vliet, *Modern Blast Furnace Ironmaking: An Introduction*, 2nd ed., IOS Press BV: Amsterdam, The Netherlands, **2009**.
[2] W. B. U. Tanzil, P. Zulli, J.M. Burgess, W. V. Pinczewski, *Trans. Iron Steel Inst. Jpn.* **1984**, *24*, 197.
[3] W. B. U. Tanzil, *Ph.D. Thesis*, University of New South Wales, Sydney, Australia, **1985**.
[4] P. Zulli, *Ph.D. Thesis*, University of New South Wales, Sydney, Australia, **1991**.
[5] L. Shao, H. Saxén, *Ind. Eng. Chem. Res.* **2013**, *52*, 5479.
[6] L. Shao, H. Saxén, *ISIJ Int.* **2011**, *51*, 1014.
[7] Q. He, P. Zulu, G.M. Evans, F. Tanzil, *Dev. Chem. Eng. Mineral Process.* **2006**, *14*, 249.
[8] R. J. Nightingale, *Ph.D. Thesis*, University of Wollongong, Wollongong, Australia, **2000**.
[9] T. Fukutake, K. Okabe, *Trans. Iron Steel Inst. Jpn.* **1976**, *16*, 317.
[10] T. Nouchi, M. Yasui, K. Takeda, *ISIJ Int.* **2003**, *43*, 175.
[11] Q. He, G. Evans, P. Zulli, F. Tanzil, *ISIJ Int.* **2012**, *52*, 774.
[12] W. Liu, L. Shao, H. Saxén, *Metals (Basel).* **2020**, *10*, 496.
[13] T. Nouchi, M. Sato, K. Takeda, T. Ariyama, *ISIJ Int.* **2005**, *45*, 1515.
[14] M. Iida, K. Ogura, T. Hakone, *ISIJ Int.* **2009**, *49*, 1123.
[15] M. Roche, M. Helle, J. van der Stel, G. Louwerse, J. Storm, H. Saxén, *Metall Mater Trans B.* **2020**, *51*, 1731.
[16] J. Brännbacka, H. Saxén, *ISIJ Int.* **2001**, *41*, 1131–1138.
[17] J. Brännbacka, H. Saxén, *Chem. Eng. Sci.* **2004**, *59*, 3423.
[18] M. Roche, M. Helle, J. van der Stel, G. Louwerse, L. Shao, H. Saxén, *Steel Res. Int.* **2019**, *90*, 1800420.
[19] K. Nishioka, T. Maeda, M. Shimizu, *ISIJ Int.* **2005**, *45*, 669.
[20] K. Nishioka, T. Maeda, M. Siiimizu, *ISIJ Int.* **2005**, *45*, 1496.
[21] G.M. Park, D.J. Lee, J.H. Lee, H.S. Yoon, *J. Comput. Fluids Eng.* **2016**, *21*, 110.
[22] H.S. Yoon, K.M. Park, Behavior of the free surface of two-phase fluid flow near the taphole in a tank, Symmetry (Basel). **2021**, *13*, 875.
[23] Y. Kaymak, T. Hauck, R. Lin, H. Rausch, COMSOL Conf. 2017 Rotterdam, **2017**.
[24] M. Vångö, S. Pirker, T. Lichtenegger, *Appl. Math. Model.* **2018**, *56*, 501.
[25] W. Liu, D.N. Mondal, A. Hermanson, L. Shao, H. Saxén, *Ironmak. Steelmak.* **2021**, *48*, 263.
[26] W. Liu, L. Shao, H. Saxén, *Steel Res. Int.* **2021**, *92*, 2100142.
[27] N. Tsuchiya, T. Fukutake, Y. Yamauchi, T. Matsumoto, *ISIJ Int.* **1998**, *38*, 116.